Soliton-mediated magnetic reversal in an all-oxide-based synthetic antiferromagnetic superlattice

Kexuan Zhang[1, 2], Kirill Zhernenkov[2], Thomas Saerbeck[3], Artur Glavic[4], Lili Qu[1], Christy J. Kinane[5], Andrew J. Caruana[5], Enda Hua[1], Guanyin Gao[1], Feng Jin[1], Binghui Ge[6], Feng Cheng[6], Sabine Pütter[2], Alexandros Koutsioubas[2], Stefan Mattauch[2], Thomas Brueckel[7], Yixi Su[*2], Lingfei Wang[*1], and Wenbin Wu[*1, 8]

1. Hefei National Laboratory for Physical Sciences at Microscale, University of Science and Technology of China, Hefei 230026, China

2. Jülich Centre for Neutron Science JCNS at Heinz Maier-Leibnitz Zentrum, Forschungszentrum Jülich, Lichtenbergstr. 1, D-85747 Garching, Germany

3. Institut Laue-Langevin, 71 Avenue des Martyrs, CS 20156, 38042 Grenoble Cedex 9, France

4. Laboratory for Neutron and Muon Instrumentation, Paul Scherrer Institut, 5232 Villigen PSI, Switzerland

5. ISIS Neutron and Muon Source, Science and Technology Facilities Council, Rutherford Appleton Laboratory, Harwell Oxford, Didcot, OX11 0QX, United Kingdom

6. Institutes of Physical Science and Information Technology, Anhui University, Hefei 230601, China

7. Jülich Centre for Neutron Science (JCNS-2) and Peter Grünberg Institute (PGI-4), Forschungszentrum Jülich GmbH, 52425 Jülich, Germany

8. Anhui Key Laboratory of Condensed Matter Physics at Extreme Conditions, High Magnetic Field Laboratory, HFIPS, Anhui, Chinese Academy of Sciences, Hefei 230031, China

ABSTRACT: All-oxide-based synthetic antiferromagnets (SAFs) are attracting intense research interest due to their superior tunability and great potentials for antiferromagnetic spintronic devices. In this work, using $La_{2/3}Ca_{1/3}MnO_3/CaRu_{1/2}Ti_{1/2}O_3$ (LCMO/CRTO) superlattice as a model SAF, we investigated the layer-resolved magnetic reversal mechanism by polarized neutron reflectivity (PNR). We found that the reversal of LCMO layer moments is mediated by nucleation, expansion, and shrinkage of a magnetic soliton. This unique magnetic reversal process creates a reversed magnetic configuration of the SAF after a simple field cycling. Therefore, it can enable a vertical data transfer from the bottom to the top of the superlattice. The physical origin of this intriguing magnetic reversal process could be attributed to the cooperation of the surface spin-flop effect and enhanced uniaxial magnetic anisotropy of the bottom LCMO layer. This work may pave a way to utilize all-oxide-based SAF for 3-dimensional spintronic devices with vertical data transfer and high-density data storage.

KEYWORDS: *Synthetic antiferromagnets, Polarized neutron reflectivity, Neutron scattering, Interlayer exchange coupling, Magnetic thin films, Oxide superlattices, in-plane anisotropy*

INTRODUCTION

Multi-layered synthetic antiferromagnets (SAF) have been extensively studied as a promising candidate for next-generation spintronic memory and logic devices.[1, 2, 3] A typical SAF usually consists of alternatively stacked ferromagnetic (FM) layers and non-magnetic spacer layers. The nature of antiferromagnetic (AF) interlayer exchange coupling (IEC) between the FM layers highly depends on the metallicity of the spacer layer.[4] For instance, in the CoFeB/Ru/CoFeB SAF system, the metallic Ru layer can trigger antiferromagnetic coupling of CoFeB layers through Ruderman-Kittel-Kasuya-Yosida-like (RKKY-like) exchange interaction.[5, 6] By contrast, in the Fe/MgO/Fe SAF system, the spin-polarized tunneling through the insulating MgO turns out to be the origin of antiferromagnetic interlayer coupling.[7, 8]

In addition to the metal/alloy-based SAFs, all-oxide-based SAFs were recently realized in an epitaxially-grown manganite/ruthenate superlattice (SL).[9] In this epitaxial system, FM $La_{2/3}Ca_{1/3}MnO_3$ (LCMO) layers were separated by non-magnetic $CaRu_{1/2}Ti_{1/2}O_3$ (CRTO) spacers.[10] The non-magnetic CRTO spacers not only trigger an AF-IEC between the LCMO layers but also enhance the T_C of ultrathin LCMO layers via interfacial charge transfer.[10, 11] Because of the intimate interplays between spin, lattice, orbital, and charge degrees of freedom, all-oxide-based SAFs potentially have superior tunability compared to the alloy/metal-based counterparts.[12] However, the layer-resolved magnetic reversal mechanism of all-oxide SAFs remains elusive. During the cycling of the external magnetic field (H), the LCMO/CRTO SL gradually exhibits an AF ground state, an intermediate (IM) state, and a saturated FM state.[9,10,11] The magnetic configurations of the IM states are unclear but particularly intriguing. Clarifying the microscopic magnetic structure of these magnetic states not only leads to a deeper understanding of the switching dynamics of the SAF but also paves a new way for designing all-oxide-based spintronic devices.

In this work, using polarized neutron reflectivity (PNR) as a probe, we have explored the layer-resolved magnetization reversal mechanism of the LCMO/CRTO SAF. PNR characterization acquires the scattering contrast of polarized neutrons across interfaces and therefore possesses high interfacial/surface sensitivity.[13, 14, 15] Therefore, PNR is effective to detect depth-resolved magnetic structures in thin films and heterostructures. Using this powerful tool, we have determined the microscopic magnetic configurations of the LCMO/CRTO SL. More interestingly, we found that the reversal of LCMO layer moments in this SAF under external H cycling is mediated by nucleation, expansion, and shrinkage of a magnetic soliton. The soliton-mediated unique magnetic reversal process can realize a vertical data transfer from the bottom to the top of the SAF. Hence, our work provides a new strategy for designing 3-dimensional AF spintronic devices via all-oxide-based SAF.[16]

EXPERIMENTAL SECTION

Fabrication of the sample. The LCMO/CRTO SL was epitaxially grown on the 001-oriented $NdGaO_3$ [NGO(001)] substrate using pulsed laser deposition (PLD). By carefully monitoring the growth rate, the thickness of LCMO and CRTO layers was fixed to 7 unit-cells (u.c.) (~2.8 nm) and 3 u.c. (~1.2 nm), respectively. The growth of LCMO/CRTO bilayers was repeated by 10 times, resulting in an LCMO/CRTO SL [denoted as $(LCMO/CRTO)_{10}$]. An additional CRTO layer of 3 u.c. thick was capped on the topmost LCMO layer. Using this

stacking sequence (inset of Figure 1a), we can ensure that each LCMO layer in the SL shares the same chemical and structural boundary conditions.

Characterization methods. The magnetic properties were measured on a Vibrating-sample magnetometer (VSM). X-ray reflectivity (XRR) was carried out on a Bruker D8 XRR instrument with CuK alpha and 2 Goebel mirrors for parallel beam optics. HAADF/STEM images were performed on an FEI Titan Themis Z microscope equipped with a probe-forming aberration corrector and operated at 300 kV. The PNR experiments was carried out at three instruments, that is, D17 at Institut Laue-Langevin (ILL) in France[17, 18], MARIA at the Heinz Maier-Leibnitz Zentrum (MLZ) in Germany[19, 20] and POLREF at ISIS Neutron and Muon Source in the U.K.[21]

Fittings and simulations of the XRR and PNR data. The fittings and simulations of the XRR and PNR data were performed using package GenX. The combination of XRR and PNR fitting is important to minimize the error produced by simulation. We determined the structural parameters by XRR and applied them to the PNR fitting process. Therefore, the magnetic parameters obtained by PNR fitting become more reliable.

RESULTS AND DISCUSSION

We first characterize the epitaxial quality and structural parameters of the LCMO/CRTO SL. Figure 1a shows the specular X-ray reflectivity (XRR) curve (scatter) of the LCMO/CRTO SL. The curve displays clear Kiessing fringes and sharp superlattice Bragg (SLB) peaks, demonstrating a high crystal quality and well-defined heterointerfaces in this SL.[22, 23] The best-fitted simulation curve (solid line) matches the experimental data well. The fitting results, presented in Table S1, provide a thickness of the LCMO (CRTO) layer of 28.13 (12.54) Å, consistent with the nominal values determined from the growth rate (7 and 3 u.c. for LCMO and CRTO layers, respectively). The scattering length density derived from XRR fitting can be further utilized for minimizing the uncertainty of PNR fitting. As shown in Figure 1b, the scanning transmission electron microscopy (STEM) image measured in high-angle-annular-dark-field (HAADF) mode further confirms that the SL has a coherent epitaxial structure, uniform layer thicknesses, and sharp interfaces. The interfacial interdiffusion is limited within 1 u.c.

The magnetic characterizations show that the LCMO/CRTO SL is a typical uniaxial SAF (Figure 1c). The orthorhombic NGO (001) substrate imposes a tensile strain of +0.85% along [010] axis while a compressive strain of -0.70% along the [100] axis of the LCMO.[24] This anisotropic strain state can give rise to a robust in-plane uniaxial magnetic anisotropy (IMA) along [010] axis.[25] Thus, we measured all the magnetic properties along the [010] easy axis. Note that the paramagnetic signal from the NGO substrate has been subtracted for all of the magnetic characterizations (details are shown in Figure S1 and S2). The inset of Figure 1c shows the temperature-dependent magnetization (*M*-*T*) curve measured during field-cooling the SL at 200 Oe. Consistent with our previous works, the *M*-*T* curve exhibits a clear FM transition at a Curie temperature (T_C) of 182 K.[12, 26, 27] Upon further cooling, *M* drops at 142 K, which can be defined as the AF Néel temperature (T_N). Note that we have measured the magnetic properties of a CRTO thin film and confirmed that the ultrathin CRTO thin film is non-magnetic (Figure S3). Given a negligible magnetism in the CRTO thin films, the drop in *M* signifies an AF alignment between the magnetic moments of adjacent LCMO layers.[28]

The AF coupling of LCMO layers in the SL can be further confirmed by an *M-H* loop measured at 50 K (Figure 1c). The *M-H* scans from both positive to negative (blue) and negative to positive (red) values exhibit multiple plateaus, corresponding to distinct magnetic configurations. Near zero-field, the *M* value is close to zero, suggesting an AF ground state of the SL. By contrast, as the external *H* increases over 1000 Oe, it is strong enough to reverse all LCMO moments, leading to a saturated FM state with high *M* up to ~3.1 μ_B/Mn. Note that this saturated *M* value is lower than that of bulk LCMO (3.67 μ_B/Mn), which originates from the thickness-driven degradation of ferromagnetism of the ultrathin LCMO layers.[26, 27] Between the AF ground state and the saturated FM state, we also observed two additional plateaus located at 610~810 Oe during *H* increasing (blue branch) and 330~510 Oe during *H* decreasing (red branch), denoted as the IM states. The *M* plateaus at the IM states are approximately 1/5 of saturated magnetization (M_S). We thus predict that only one LCMO layer moment reverses at the IM state, which results in 8 antiparallel-aligned LCMO layers and 2 parallel-aligned LCMO layers. However, the microscopic magnetic configuration of the IM state cannot be deduced from the magnetic characterizations. Therefore, we turn to the layer resolved magnetic characterization using PNR.

As marked in Figure 1c, we carried out PNR experiments at 6 stages during the *H* scans, and the temperature was fixed at 50 K during the PNR measurements. Stages I to IV were measured with *H* increasing from 0 to 5000 Oe, while stages V and VI were measured with *H* decreasing from 5000 to 0 Oe. According to the volume magnetometry, at stages I and II, the SL is in the AF ground state. At stages III and VI, the SL is in the IM stage. At stages IV and V, the SL is in the saturated FM stage. Specular reflectivity is measured as a function of the scattering wave vector *Qz* oriented perpendicular to the sample surface, defined as: $Q_z = \frac{4\pi}{\lambda} \sin\theta$, where θ is the incident angle of the neutron beam and λ is the wavelength of the neutron. Intensity contour plots of the reflected intensity in instrumental coordinates θ and λ are shown in Figure S4. Neither an off-specular peak nor featureless diffuse scattering in the off-specular area is observed. Hence, we can exclude the possible formation of correlated lateral magnetic domains at all the measurement stages.[29]

Before analyzing the detailed magnetic structure, we first confirm the collinear nature of magnetic moments in the LCMO/CRTO SL. We performed full-polarized PNR measurements at stages I, III, and VI. According to the fit results shown in Figure S5, the projection of the magnetization deviating from [010] direction tends to zero. Considering the polarizing efficiency of the instrument, the intensity observed in spin-flip channels (R^{+-} and R^{-+}) is a parasitic signal. Hence, within the sensitivity of the measurement, all the magnetic moments of the LCMO layers are collinearly aligned for all the stages. This is also consistent with the strong IMA of the SL. Based on this analysis, we will only show the PNR results from non-spin-flip channels (R^{++} and R^{--}) in the following part.

We first look into the simple AF ground states (stage I and II) and saturated FM states (stage IV and V). PNR data and simulation of stages I and IV are presented in Figure 2. And the results for stage II and V are included in Figure S6, which is proved to be the same as I and IV, respectively. As shown in Figure 2a,b, both the PNR curves measured from stage I and IV show a series of Kiessig fringes and an SLB peak. The SLB peak of FM states (stage IV) shares the same Q_z value as the first SLB peak observed in the XRR curve (Figure 1c). The Q_z position of the first SLB peak of stage I is nearly half of the value of stage IV. Within the first Born approximation, the intensity of Bragg reflection from a periodic array of 2*N* layers can be described as $I_0 \propto \{\sin[qd(2N)/2]/\sin qd/2\}^2$， where

d is the size of a magnetic unit cell.[30] The first local maximum of I_0 at the SLB peak appears at $q = 2\pi/d$. The relative position of the SLB peak indicates that the magnetic unit cell at stage I is doubled with respect to stage IV, which means LCMO layers ought to be coherently antiparallel-aligned at stage I. We utilized two possible models for describing the AF-coupled stage I, distinguished by the direction of the magnetic moment in each layer. In the first model, the moment of the top LCMO layer is set to be parallel to the external H (inset of Figure 2a). This model provides a reasonably good fit for the experimental results. The optimized fit matches well with the experimental PNR curve. We also tested the second model with the topmost LCMO moment antiparallel to the external H (Figure S7). This model causes inverse fits of spin-up and spin-down channels, and thus it is improper for describing the magnetic configuration of the SL. As shown in Figure 2b, a uniform FM model can fit the PNR curve of stage IV well. The depth profiles of nuclear scattering length density (NSLD) and magnetic scattering length density (MSLD) are shown in Figure 2c,d. For stage I, the fitted M values in LCMO layers are +3.52 (-0.29, +0.17) μ_B/Mn and -3.25 (-0.38, +0.37) μ_B/Mn . For stage IV, the fitted M value is +3.19 (-0.43, +0.47) μ_B/Mn, close to the M_S value obtained from M-H loops. Based on these results, the antiparallel (parallel) alignment of LCMO moments in the SL at low (high) H is experimentally confirmed by PNR measurements.

Now we turn to investigate the layer-resolved magnetic structure of the IM states, which appear as plateaus in the M-H loop at roughly 1/5 of M_S. We first look into the PNR results measured at stage III. At stage III, as shown in Figure 3a,b, the main peaks of the PNR curve have the same Q_z as the AF ground state. However, the SLB peak of the R^{--} channel shows a peak splitting. This implies a non-regular magnetic structure in depth.

Based on the analysis of the PNR results, we suggest that the magnetic configuration in stage III could be determined by a surface spin-flop (SSF) transition.[31] This is an intrinsic magnetic transition for finite SAF systems. The antiparallel-aligned layers at the ends of the SL are easier to be reversed by external H because they are magnetically coupled with only one neighboring layer. According to this SSF scenario, we speculate that the moment of either the topmost or the bottommost LCMO layer is inverted by the external H. From stage I, we have determined that only the moment of the bottommost LCMO aligns antiparallel to the external H. Therefore, for model 1 at stage III, we hypothesize that the SSF occurs at the bottommost LCMO layer. Figure 3a shows the PNR curves and optimized fits curve based on model 1, which shows only a small deviation from the experimental curves and leads to a reasonable MSLD profile (Figure 3c). The fitted local M values in bottom-most 2 layers are +3.29 (-0.56, +0.35) μ_B/Mn, and in the AFM part they are -3.49 (-0.37, +0.34) and +3.89 (-0.48, +0.11) μ_B/Mn. For comparison, we also applied another model (model 2) where one interior LCMO layer is reversed (the second layer from the top, shown in Figure 3b. Compared to the fits using model 1, the optimized fitting curves from model 2 show much larger deviations from the experimental curves. The corresponding MSLD profile (Figure 3d) also changes dramatically: the local M values for the top 2 LCMO layers are close to zero, and the M values of the bottom 8 layers are -2.34 (-0.48, +0.09) and +5.00 (-0.53, +0.37) μ_B/Mn. These values are outside the physically reasonable range for the magnetization within LCMO layers. Therefore, these asymmetric and unreasonable fit results suggest that model 1 is proper for describing the magnetic configuration in stage III, confirming the situation that was expected based on the SSF scenario. In other words, by increasing H, the SSF enables magnetic soliton nucleation near the SL/substrate interface.

Following similar procedures, we further investigated the magnetic configuration at stage VI. The PNR curve taken at stage VI is shown in Figure 3e,f. Although the *M* values at stages III and VI are almost identical, the PNR curves from R^{++} and R^{--} channels appear to be inverted. As aforementioned, inversed fits were obtained by model 2 applied for stage I (Figure S4). Therefore, we set 2 models based on that to simulate the PNR curves of stage VI. For model 1, the two bottom LCMO layers are set to be parallel to external *H* (Figure 3e). And for model 2, the top two LCMO layers remain parallel to the external *H* (Figure 3f). As shown in Figure 3e-h, model 2 can provide a much better fit than model 1, thus it appears suitable to describe the magnetic configuration at stage VI. Fits based on model 2 result in a more reasonable MSLD profile (Figure 3g,h). These results confirm that the two IM states (stage III and VI) have distinct layer-resolved magnetic profiles, though they are indistinguishable from the *M-H* curve.

The layer-resolved magnetic profile of the LCMO/CRTO SAF system at the AF ground states, IM states, and saturated FM states show a distinct evolution of magnetic configurations in the SL. As summarized in Figure 4. The 2 parallel-aligned LCMO layers in IM states can be seen as an achiral soliton embedded in a finite SAF chain.[32, 33] The evolution of magnetic configurations of the SL can be regarded as a vertical propagation of the magnetic soliton along the finite SAF. Specifically, as *H* increases from zero to 470 Oe, the SSF makes the moment of the bottom LCMO layer reverses first, leading to nucleation of a magnetic soliton at the bottom of the SAF. By further increasing *H* to 810 Oe and above, a bulk spin-flop (BSF) process aligns all the LCMO layers to *H*, which can be described as a soliton expansion to the whole SAF chain. As *H* decreases from 5000 to 696 Oe, on the contrary, the moments of the top 2 LCMO layers remain unchanged when the moments in the rest layers restore to antiparallel-alignment. This process can be seen as shrinkage of the magnetic soliton at the top of SAF. By further decreasing *H*, the entire SL restores to AF ground state. Notably, comparing with the AF ground state before the *H* cycling process, the moment of the top LCMO layer becomes reversed. This means that the soliton behavior results in a vertical data transfer from the bottom to the top of the SAF.

The most unique spin-flop step during the *H* cycling is the soliton shrinkage process. Starting from the saturated FM state, as *H* decreases, the soliton can shrink at either the top or the bottom of the SL and eventually results in two AF ground states with different magnetic configurations. Nevertheless, we only observed the top-shrinkage of magnetic soliton experimentally. At the final AF state, the bottom LCMO moment remains parallel to the external *H*, while the top LCMO moment eventually reverses and aligns antiparallel to *H*. Accordingly, we speculate that the bottommost LCMO layer has a larger local coercive field, which is determined by both IEC and IMA. Since the topmost and bottommost LCMO have the same IEC strength, we suggest that the IMA for the bottommost LCMO should be stronger.

The magnetic anisotropy of manganite is determined by both strain and octahedral distortion patterns. Using in-plane strain mapping from STEM measurements, we observe that all the LCMO layers are nearly in the same strain state (Figure S8). On this basis, we suggest that the stronger IMA of the bottommost LCMO is induced by interfacial-coupling of oxygen octahedral distortion with NGO(001) substrate and bottom CRTO layer.[34] The length-scale of octahedral interfacial coupling is commonly within several nanometers. Hence, its influence should be localized within the bottommost LCMO layer.[35] The NGO(001) substrate has strong octahedral tilting along the

[010] axis. It could pass through the 3 u.c.-thick CRTO layer and transfer into the bottommost LCMO layer. The enhanced octahedral tilting can result in a stronger IMA and thus larger coercive field.[36] Therefore, as *H* decreases, the bottommost LCMO layer is pinned to the *H* direction, resulting in the propagation of magnetic soliton from the bottom to the top of the SAF.

CONCLUSIONS

In conclusion, we have revealed the microscopic magnetization reversal mechanism in the LCMO/CRTO SAF by PNR characterization. The layer-resolved magnetic reversal process is mediated by nucleation, expansion, and shrinkage of a magnetic soliton. This unique evolution of magnetic configurations could be attributed to the cooperation of a spatial variation of IMA along the out-of-plane direction and the SSF effect. As a result, vertical data transfer is spontaneously realized in this system.

Our work revealed the high sensitivity of reversal sequence to the strength ratio between IMA and IEC in an all-oxide SAF. The IMA and IEC in oxide multilayers can be effectively modulated via strain, layer thickness, chemical doping, interfacial structure, etc.[37] Therefore, it is technically promising to engineer the reversal process of oxide SAF systems at a microscopic scale and incorporate them in spintronic devices with designed functionalities.[38, 39] Accordingly, our work paves a new strategy for incorporating all-oxide-based SAF systems in designed functionalities and geometry, especially for the 3-dimensional spintronic memory and logic devices with high integration level.

ASSOCIATED CONTENT

Supporting Information

Additional information is available regarding the materials and methods, instrumentation, details on fitting process of X-ray reflectivity and polarized neutron reflectivity, Figure S1 to S10. (PDF)

AUTHOR INFORMATION

Corresponding Authors

Yixi Su - *Jülich Centre for Neutron Science JCNS at Heinz Maier-Leibnitz Zentrum, Forschungszentrum Jülich, Lichtenbergstr. 1, D-85747 Garching, Germany;*

Email: y.su@fz-juelich.de

Lingfei Wang - *Hefei National Laboratory for Physical Sciences at Microscale, University of Science and Technology of China, Hefei 230026, China;*

Email: wanglf@ustc.edu.cn

Wenbin Wu - *Hefei National Laboratory for Physical Sciences at Microscale, University of Science and Technology of China, Hefei 230026, China;*

Anhui Key Laboratory of Condensed Matter Physics at Extreme Conditions, High Magnetic Field Laboratory, HFIPS, Anhui, Chinese Academy of Sciences, Hefei 230031, China;

Email: wuwb@ustc.edu.cn

Authors

Kexuan Zhang - *Hefei National Laboratory for Physical Sciences at Microscale, University of Science and Technology of China, Hefei 230026, China; Jülich Centre for Neutron Science JCNS at Heinz Maier-Leibnitz Zentrum, Forschungszentrum Jülich, Lichtenbergstr. 1, D-85747 Garching, Germany*

Kirill Zhernenkov - *Jülich Centre for Neutron Science JCNS at Heinz Maier-Leibnitz Zentrum, Forschungszentrum Jülich, Lichtenbergstr. 1, D-85747 Garching, Germany*

Thomas Saerbeck - *Institut Laue-Langevin, 71 Avenue des Martyrs, CS 20156, 38042 Grenoble Cedex 9, France*

Artur Glavic - *Laboratory for Neutron and Muon Instrumentation, Paul Scherrer Institut, 5232 Villigen PSI, Switzerland*

Lili Qu - *Hefei National Laboratory for Physical Sciences at Microscale, University of Science and Technology of China, Hefei 230026, China*

Christy J. Kinane - *ISIS Neutron and Muon Source, Science and Technology Facilities Council, Rutherford Appleton Laboratory, Harwell Oxford, Didcot, OX11 0QX, United Kingdom*

Andrew J. Caruana - *ISIS Neutron and Muon Source, Science and Technology Facilities Council, Rutherford Appleton Laboratory, Harwell Oxford, Didcot, OX11 0QX, United Kingdom*

Enda Hua - *Hefei National Laboratory for Physical Sciences at Microscale, University of Science and Technology of China, Hefei 230026, China*

Guanyin Gao - *Hefei National Laboratory for Physical Sciences at Microscale, University of Science and Technology of China, Hefei 230026, China*

Feng Jin - *Hefei National Laboratory for Physical Sciences at Microscale, University of Science and Technology of China, Hefei 230026, China*

Binghui Ge - *Institutes of Physical Science and Information Technology, Anhui University, Hefei 230601, China*

Feng Cheng - *Institutes of Physical Science and Information Technology, Anhui University, Hefei 230601, China*

Sabine Pütter - *Jülich Centre for Neutron Science JCNS at Heinz Maier-Leibnitz Zentrum, Forschungszentrum Jülich, Lichtenbergstr. 1, D-85747 Garching, Germany*

Alexandros Koutsioubas - *Jülich Centre for Neutron Science JCNS at Heinz Maier-Leibnitz Zentrum, Forschungszentrum Jülich, Lichtenbergstr. 1, D-85747 Garching, Germany*

Stefan Mattauch - *Jülich Centre for Neutron Science JCNS at Heinz Maier-Leibnitz Zentrum, Forschungszentrum Jülich, Lichtenbergstr. 1, D-85747 Garching, Germany*

Thomas Brueckel - *Jülich Centre for Neutron Science (JCNS-2) and Peter Grünberg Institute (PGI-4), Forschungszentrum Jülich GmbH, 52425 Jülich, Germany*

Author Contributions

K. Z. (K. Zhang), Y.S., L. W. and W.W**.** conceived the experiments and prepared the manuscript. K. Z. (K. Zhernenkov) assisted the PNR experiments at D17, MARIA and POLREF. T.S. was responsible for the PNR

experiment at D17, and helped to analyze the data. A.G. offered tutorial on PNR simulation with GenX package. C.J.K. and A.J.C. were responsible for the PNR experiment at POLREF. L.Q., E.H. and F.J. helped with sample preparation. G.G. and S.P. carried out XRR measurements. F.C. and B.G. performed STEM measurements. A.K., S.M. and T.B. supervised and performed PNR measurements at MARIA. All authors were involved in the analysis and discussion of the experimental results.

Funding Sources

This work was supported by the National Basic Research Program of China (Grant Nos. 2016YFA0401003, 2017YFA0403502, and No. 2020YFA0309100), the National Natural Science Foundation of China (Grant Nos. 11974326, 12074365, 11804342, U2032218 and 51872278), the Fundamental Research Funds for the Central Universities (WK2030000035), and Hefei Science Center of Chinese Academy of Sciences (Grant No. 2020HSC-UE014). The international cooperation was supported by China Scholarship Council for 1 year's study at Jülich Center for Neutron Science at MLZ.

Notes

The authors declare no competing financial interest.

ACKNOWLEDGMENT

The PNR measurements presented in this manuscript were conducted on the polarized neutron reflectometer D17 at the Institute Laue-Langevin, France (DOI:10.5291/ILL-DATA.5-31-2697), MARIA at the Heinz Maier-Leibnitz Zentrum (MLZ), Germany (Proposal ID: 16332) and POLREF at ISIS, UK (DOI: 10.5286/ISIS.E.RB2010201). We appreciate the great support from all these neutron facilities. The experiment data and analysis from MARIA and POLREF are presented in Supporting information.

ABBREVIATIONS

SAF, all-oxide-based synthetic antiferromagnet; LCMO, $La_{2/3}Ca_{1/3}MnO_3$; CRTO, $CaRu_{1/2}Ti_{1/2}O_3$; FM, ferromagnetic; AF, antiferromagnetic; IEC, interlayer exchange coupling; RKKY-like, Ruderman-Kittel-Kasuya-Yosida-like; SL, superlattice; IM, intermediate; PNR, polarized neutron reflectivity; NGO, $NdGaO_3$; PLD, pulsed laser deposition; XRR, X-ray reflectivity; SLB, superlattice Bragg; STEM, scanning transmission electron microscopy; HAADF, high-angle-annular-dark-field; IMA, in-plane uniaxial magnetic anisotropy; NSLD, nuclear scattering length density; MSLD, magnetic scattering length density; SSF, surface spin-flop; BSF, bulk spin-flop.

REFERENCES

(1) Duine, R. A.; Lee, K.-J.; Parkin, S. S. P.; Stiles, M. D. Synthetic Antiferromagnetic Spintronics. *Nat. Phys.* **2018,** *14*, 217-219.

(2) Lavrijsen, R.; Lee, J. H.; Fernandez-Pacheco, A.; Petit, D. C.; Mansell, R.; Cowburn, R. P. Magnetic Ratchet for Three-dimensional Spintronic Memory and Logic. *Nature* **2013,** *493*, 647-650.

(3) Sbiaa, R.; Meng, H.; Piramanayagam, S. N. Materials with Perpendicular Magnetic Anisotropy for Magnetic Random Access Memory. *Phys. Status Solidi-Rapid Res. Lett.* **2011,** *5*, 413-419.

(4) Stiles, M. D. Interlayer Exchange Coupling. In *Ultrathin Magnetic Structures III: Fundamentals of Nanomagnetism*, Bland, J. A. C.; Heinrich, B., Eds. Springer Berlin Heidelberg: Berlin, Heidelberg, **2005**, 99-142.

(5) Bruno, P.; Chappert, C. Oscillatory Coupling between Ferromagnetic Layers Separated by a Nonmagnetic Metal Spacer. *Phys. Rev. Lett.* **1991,** *67*, 1602-1605.

(6) Yang, Q.; Wang, L.; Zhou, Z.; Wang, L.; Zhang, Y.; Zhao, S.; Dong, G.; Cheng, Y.; Min, T.; Hu, Z. Ionic Liquid Gating Control of RKKY Interaction in FeCoB/Ru/FeCoB and $(Pt/Co)_2/Ru/(Co/Pt)_2$ Multilayers. *Nat. Commun.* **2018,** *9*, article no. 911.

(7) Faure-Vincent, J.; Bellouard, C. T.; Popova, E.; Hehn, M.; Montaigne, F.; Schuhl, A. Interlayer Magnetic Coupling Interactions of Two Ferromagnetic Layers by Spin Polarized Tunneling. *Phys. Rev. Lett.* **2002,** *89*, article no. 107206.

(8) Tiusan, C.; Faure-Vincent, J.; Bellouard, C.; Hehn, M.; Jouguelet, E.; Schuhl, A. Interfacial Resonance State Probed by Spin-polarized Tunneling in Epitaxial Fe/MgO/Fe Tunnel Junctions. *Phys. Rev. Lett.* **2004,** *93*, article no. 106602.

(9) Chen, B.; Xu, H.; Ma, C.; Mattauch, S.; Lan, D.; Jin, F.; Guo, Z.; Wan, S.; Chen, P.; Gao, G.; Chen, F.; Su, Y.; Wu, W. All-oxide–based Synthetic Antiferromagnets Exhibiting Layer-resolved Magnetization Reversal. *Science* **2017,** *357*, 191-194.

(10) Lan, D.; Chen, B.; Qu, L.; Zhang, K.; Xu, L.; Jin, F.; Guo, Z.; Chen, F.; Gao, G.; Wu, W. Tuning Antiferromagnetic Interlayer Exchange Coupling in $La_{0.67}Ca_{0.33}MnO_3$-based Synthetic Antiferromagnets. *APL Mater.* **2019,** *7*, article no. 031119.

(11) Xu, H.; Wan, S.; Chen, B.; Ma, C.; Jin, F.; Guo, Z.; Lan, D.; Chen, F.; Wu, W. Antiferromagnetic Interlayer Exchange Coupling in All-perovskite $La_{0.7}Sr_{0.3}MnO_3/SrRu_{1-x}Ti_xO_3$ superlattices. *Appl. Phys. Lett.* **2017,** *110*, article no. 082402.

(12) Ramesh, R.; Schlom, D. G. Creating Emergent Phenomena in Oxide Superlattices. *Nat. Rev. Mater.* **2019**, *4*, 257-268.

(13) Fitzsimmons, M. R.; Bader, S. D.; Borchers, J. A.; Felcher, G. P.; Furdyna, J. K.; Hoffmann, A.; Kortright, J. B.; Schuller, I. K.; Schulthess, T. C.; Sinha, S. K.; Toney, M. F.; Weller, D.; Wolf, S. Neutron Scattering Studies of Nanomagnetism and Artificially Structured Materials. *J. Magn. Magn. Mater.* **2004,** *271*, 103-146.

(14) Fitzsimmons, M.; Schuller, I. K. Neutron scattering—The Key Characterization Tool for Nanostructured Magnetic Materials. *J. Magn. Magn. Mater.* **2014,** *350*, 199-208.

(15) Liu, Y.; Ke, X. Interfacial Magnetism in Complex Oxide Heterostructures Probed by Neutrons and X-rays. *J. Phys.-Condes. Matter* **2015,** *27*, article no. 373003.

(16) Fernandez-Pacheco, A.; Streubel, R.; Fruchart, O.; Hertel, R.; Fischer, P.; Cowburn, R. P. Three-dimensional Nanomagnetism. *Nat. Commun.* **2017,** *8*, article no. 15756.

(17) T. Saerbeck, R. Cubitt, A. Wildes, G. Manzin, K.H. Andersen, P. Gutfreund. Recent Upgrades of the Neutron Reflectometer D17 at ILL. *J. Appl. Crystallogr.***2018**, *51*, 249-256.

(18) Kexuan Zhang; Brueckel Thomas; Mattauch Stefan; Saerbeck Thomas; Su Yixi and Zhernenkov Kirill. Study of the Magnetization Reversal Mechanism in Antiferromagnetic Interlayer Exchange Coupling in $LaCaMnO_3/CaRuTiO_3$ Superlattices. Data set; Institut Laue-Langevin (ILL) **2020**, doi:10.5291/ILL-DATA.5-31-2697.

(19) Mattauch, S., Koutsioubas, A., Rücker, U., Korolkov, D., Fracassi, V., Daemen, J., Schmitz, R., Bussmann, K., Suxdorf, F., Wagener, M. and Kämmerling, P. The High-intensity Reflectometer of the Jülich Centre for Neutron Science: MARIA. *J. Appl. Crystallogr.* **2018**, *51*, 646-654.

(20) Mattauch, S., Koutsioubas, A. and Pütter, S. *J. large-scale res. facil.* **2015**, *1*, A8.

(21) Yixi, S.; Kexuan Z.; Stefan M.; Thomas B. Study of the Magnetization Reversal Mechanism in Antiferromagnetic Interlayer Exchange Coupling in $LaCaMnO_3/CaRuTiO_3$ Superlattices. Data set; STFC ISIS Neutron and Muon Source, **2020**, https://doi.org/10.5286/ISIS.E.RB2010201.

(22) Kiessig, H. Untersuchungen zur Totalreflexion von Röntgenstrahlen. *Annalen der Physik*, **1931**, *402*(6), 715-768.

(23)Uribe-Laverde, M. A.; Satapathy, D. K.; Marozau, I.; Malik, V. K.; Das, S.; Sen, K.; Stahn, J.; Rühm, A.; Kim, J. H.; Keller, T.; Devishvili, A.; Toperverg, B. P.; Bernhard, C. Depth Profile of the Ferromagnetic Order in a $YBa_2Cu_3O_7/La_{2/3}Ca_{1/3}MnO_3$ Superlattice on a LSAT Substrate: A Polarized Neutron Reflectometry Study. *Phys. Rev. B* **2013,** *87*, article no. 115105.

(24) Wang, L. F.; Huang, Z.; Tan, X. L.; Chen, P. F.; Zhi, B. W.; Li, G. M.; Wu, W. B. Pseudomorphic Strain Induced Strong Anisotropic Magnetoresistance over a Wide Temperature Range in Epitaxial $La_{0.67}Ca_{0.33}MnO_3/NdGaO_3(001)$ Films. *Appl. Phys. Lett.* **2010,** *97*, article no. 242507.

(25) Jin, F.; Gu, M.; Ma, C.; Guo, E. J.; Zhu, J.; Qu, L.; Zhang, Z.; Zhang, K.; Xu, L.; Chen, B.; Chen, F.; Gao, G.; Rondinelli, J. M.; Wu, W. Uniaxial Strain-Controlled Ground States in Manganite Films. *Nano Lett.* **2020,** *20*, 1131-1140.

(26) Chen, B.; Chen, P.; Xu, H.; Jin, F.; Guo, Z.; Lan, D.; Wan, S.; Gao, G.; Chen, F.; Wu, W. Interfacial Control of Ferromagnetism in Ultrathin $La_{0.67}Ca_{0.33}MnO_3$ Sandwiched between $CaRu_{1-x}Ti_xO_3$ (x = 0-0.8) Epilayers. *ACS Appl. Mater. Inter.* **2016,** *8*, 34924-34932.

(27) Chen, B. B.; Chen, P. F.; Xu, H. R.; Tan, X. L.; Jin, F.; Guo, Z.; Zhi, B. W.; Wu, W. B. Contrasting Size-scaling Behavior of Ferromagnetism in $La_{0.67}Ca_{0.33}MnO_3$ Films and $La_{0.67}Ca_{0.33}MnO_3/CaRuO_3$ Multilayers. *Appl. Phys. Lett.* **2014,** *104*, article no. 242416.

(28) He, T.; Cava, R. J. Disorder-induced Ferromagnetism in $CaRuO_3$. *Phys. Rev. B* **2001,** *63*, article no. 172403.

(29) Paul, A.; Buchmeier, M.; Bürgler, D. E.; Rücker, U.; Schneider, C. M. Twisted Magnetization State at the Interface of an Antiferromagnetically Coupled Fe/Si Multilayer as Probed by Specular and Off-specular Polarized Neutron Scattering. *Phys. Rev. B* **2008,** *77*, article no. 184409.

(30) te Velthuis, S. G.; Jiang, J. S.; Bader, S. D.; Felcher, G. P. Spin Flop Transition in a Finite Antiferromagnetic Superlattice: Evolution of the Magnetic Structure. *Phys. Rev. Lett.* **2002,** *89*, article no. 127203.

(31) Rößler, U. K.; Bogdanov, A. N. Reorientation in Antiferromagnetic Multilayers: Spin-flop Transition and Surface Effects. *Phys. Stat. Sol. (c)* **2004,** *1*, 3297-3305.

(32) Fernández-Pacheco, A.; Steinke, N. J.; Mahendru, D.; Welbourne, A.; Mansell, R.; Chin, S. L.; Petit, D.; Lee, J.; Dalgliesh, R.; Langridge, S.; Cowburn, R. P. Magnetic State of Multilayered Synthetic Antiferromagnets during Soliton Nucleation and Propagation for Vertical Data Transfer. *Adv. Mater. Interfaces* **2016,** *3*, article no. 1600097.

(33) Vedmedenko, E. Y.; Altwein, D. Topologically Protected Magnetic Helix for All-spin-based Applications. *Phys. Rev. Lett.* **2014,** *112*, article no. 017206.

(34) Rondinelli, J. M.; Spaldin, N. A. Structure and Properties of Functional Oxide Thin Films: Insights from Electronic-structure Calculations. *Adv. Mater.* **2011,** *23*, 3363-3381.

(35) Moon, E. J.; Balachandran, P. V.; Kirby, B. J.; Keavney, D. J.; Sichel-Tissot, R. J.; Schleputz, C. M.; Karapetrova, E.; Cheng, X. M.; Rondinelli, J. M.; May, S. J. Effect of Interfacial Octahedral Behavior in Ultrathin sManganite Films. *Nano Lett.* **2014,** *14*, 2509-2514.

(36) Liao, Z.; Huijben, M.; Zhong, Z.; Gauquelin, N.; Macke, S.; Green, R. J.; Van Aert, S.; Verbeeck, J.; Van Tendeloo, G.; Held, K.; Sawatzky, G. A.; Koster, G.; Rijnders, G. Controlled Lateral Anisotropy in Correlated Manganite Heterostructures by Interface-engineered Oxygen Octahedral Coupling. *Nat. Mater.* **2016,** *15*, 425-431.

(37)Fernández-Pacheco, A.; Petit, D.; Mansell, R.; Lavrijsen, R.; Lee, J. H.; Cowburn, R. P. Controllable Nucleation and Propagation of Topological Magnetic Solitons in CoFeB/Ru Ferrimagnetic superlattices. *Phys. Rev. B* **2012,** *8*6, article no. 104422.

(38) Siddiqui, S. A.; Dutta, S.; Tang, A.; Liu, L.; Ross, C. A.; Baldo, M. A. Magnetic Domain Wall Based Synaptic and Activation Function Generator for Neuromorphic Accelerators. *Nano Lett.* **2020,** *20*, 1033-1040.

(39) Böhm, B.; Fallarino, L.; Pohl, D.; Rellinghaus, B.; Nielsch, K.; Kiselev, N. S.; Hellwig, O. Antiferromagnetic Domain Wall Control via Surface Spin Flop in Fully Tunable Synthetic Antiferromagnets with Perpendicular Magnetic Anisotropy. *Phys. Rev. B* **2019,** *10*0, article no. 140411.

Figures

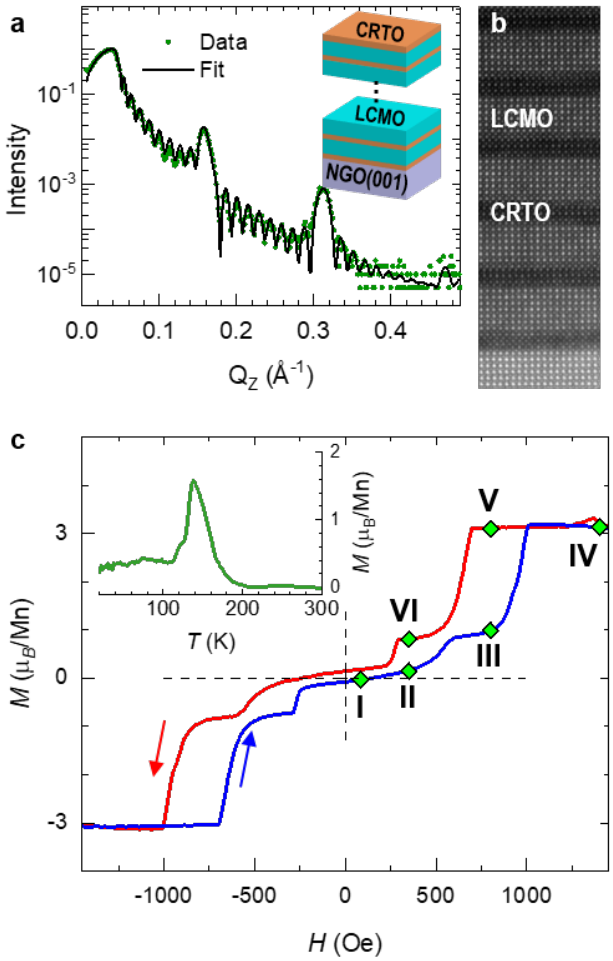

Figure 1. Structural and magnetic characterizations of LCMO/CRTO SL. (a) XRR curve measured from the LCMO/CRTO SL (scatter) together with the fit results (solid line). The inset shows a schematic stacking sequence of the SL. (b) HAADF-STEM image taken along the [110] zone-axis. (c) *M*-*H* hysteresis loop measured along the in-plane easy-axis [010] at 50 K. *H*-scanning directions are indicated by solid arrows. The inset shows the *M*-*T* curve measured under a cooling field of 200 Oe along [010] axis.

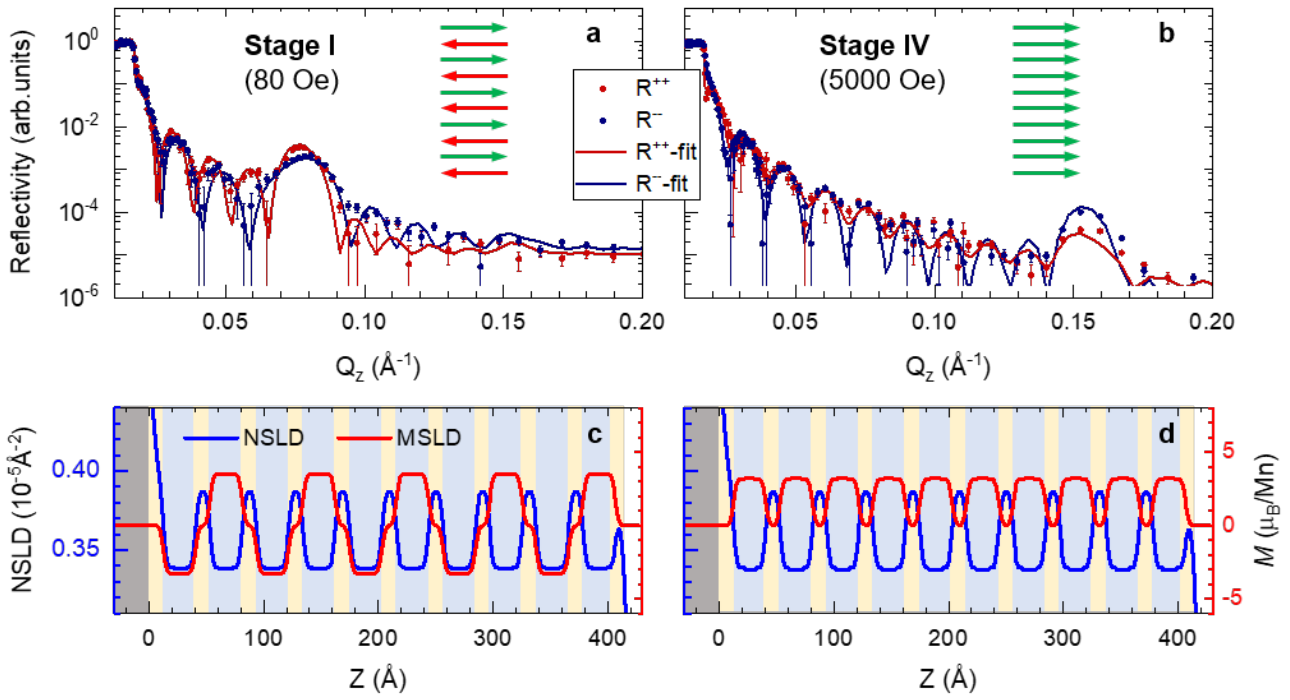

Figure 2. PNR results measured from the LCMO/CRTO SL at the initial AF ground state and saturated FM state. (a, b) PNR data (scatter) and fitting results (solid line) of the (a) AF ground state and (b) saturated FM state. The models we used are sketched in the insets. Each arrow represents a layer of LCMO. Depth profiles of NSLD and MSLD derived from best fits in (a)(b) are shown in (c)(d). Light blue, yellow, and gray-colored backgrounds represent the LCMO layers, CRTO layers, and NGO substrates, respectively.

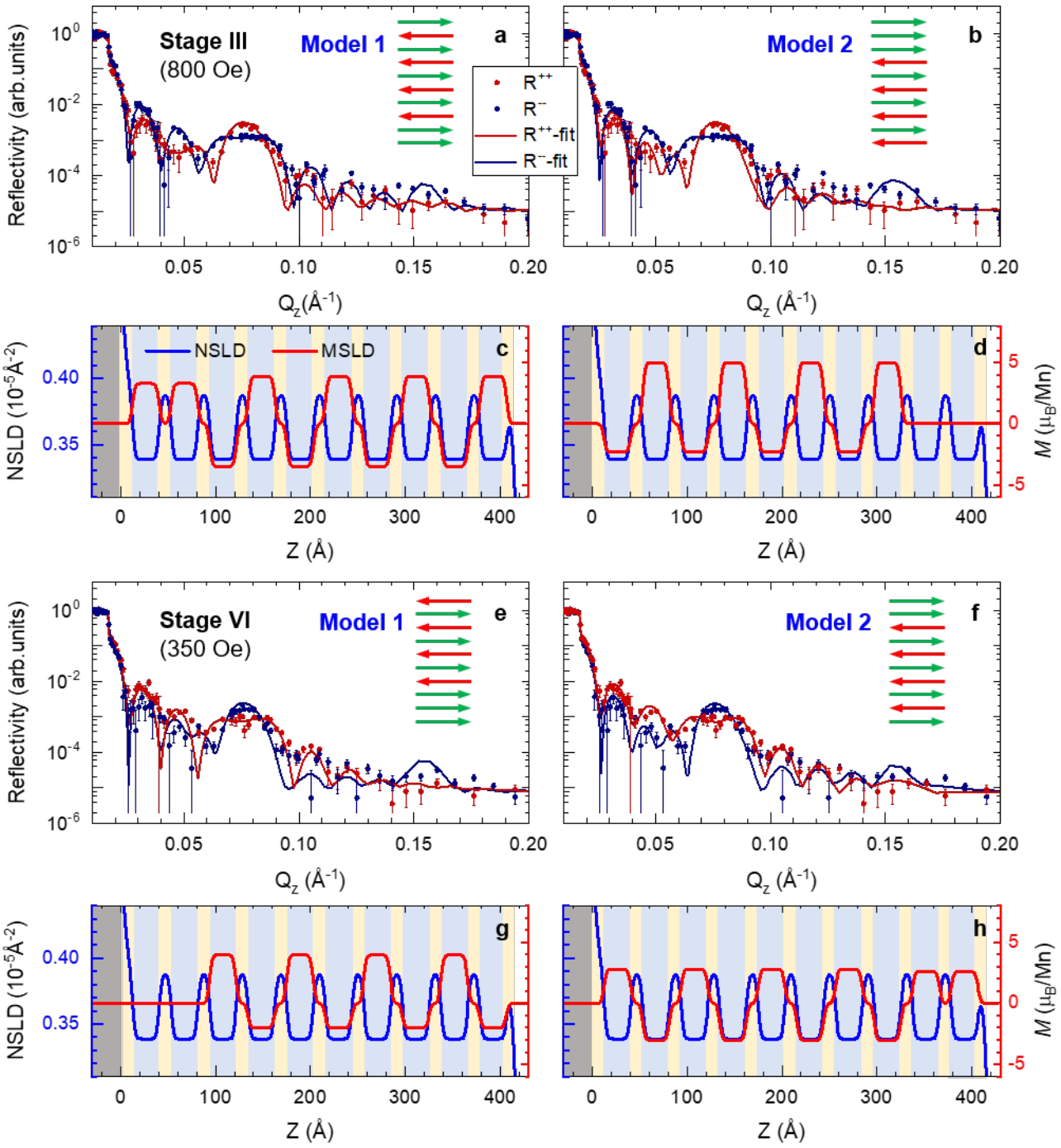

Figure 3. PNR results measured from the LCMO/CRTO SL at IM states. (a, b, e, f) PNR data (scatter) and fitting results (solid line) of the (a, b) stage III and (e, f) stage VI. The models used are sketched in the insets. Each arrow represents a layer of LCMO. Depth profiles of NSLD and MSLD derived from best fits in (a, b, e, f) are shown in (c, d, g, h), respectively. Light blue, yellow, and gray-colored backgrounds represent the LCMO layers, CRTO layers, and NGO substrates, respectively.

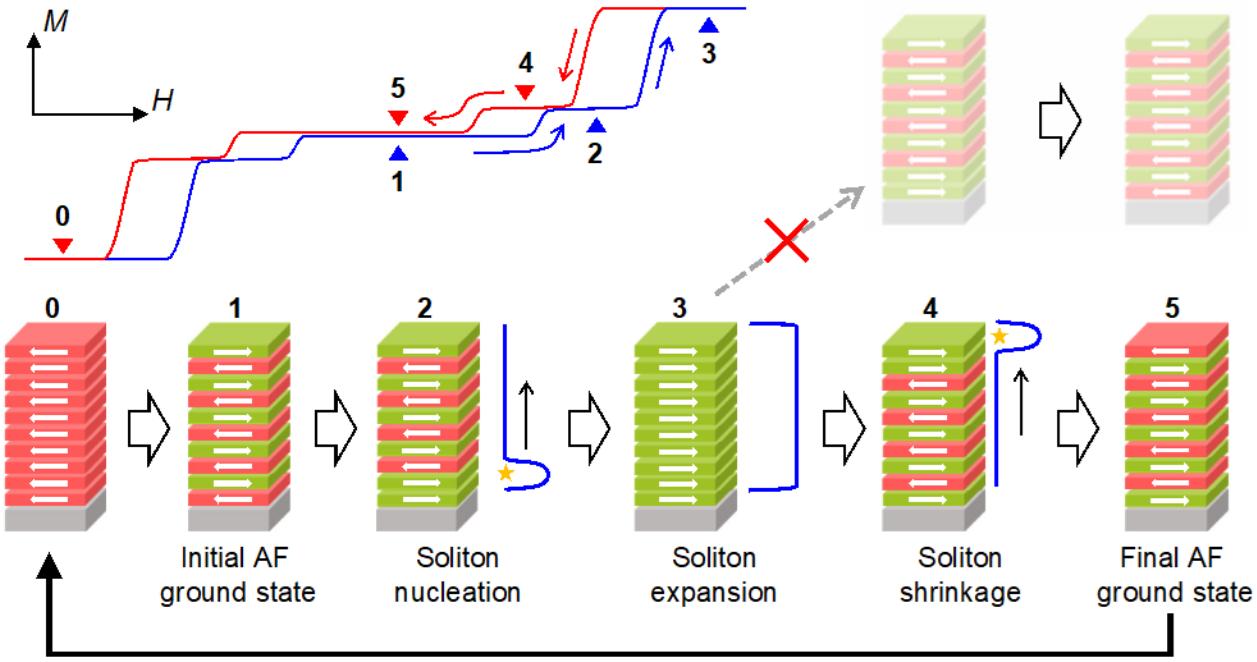

Figure 4. Layer-resolved magnetic reversal processes of the LCMO/CRTO SAF. The top-left panel is a schematic *M-H* hysteresis loop. We labeled a series of representative magnetic stages (0 to 5) by triangles, and the field scanning directions are labeled by open arrows. The layer-resolved magnetic configurations of these stages are shown in the bottom panel. The evolution from stage 2 to 4 can be seen as soliton nucleation, expansion, and shrinkage. We also display an alternative magnetic reversal path from saturated FM stage 3 to stage 5. This path was proven to be experimentally unaccessible. Therefore, the magnetic moments of all the LCMO layers in stage 5 are reversed compared to those in stage 1.

Table of Contents artwork